Chinese Chemical Letters 35 (2024) 108814

Contents lists available at ScienceDirect

Chinese Chemical Letters

journal homepage: www.elsevier.com/locate/cclet

Highly-chlorinated inert and robust interphase without mineralization of oxide enhancing high-rate Li metal batteries

Long Li[a], Kang Yang[a], Chenpeng Xi[a], Mengchao Li[a], Borong Li[a], Gui Xu[a], Yuanbin Xiao[a], Xiancai Cui[a], Zhiliang Liu[b,*], Lingyun Li[a,*], Yan Yu[a,*], Chengkai Yang[a,*]

[a] Key Laboratory of Advanced Materials Technologies, International (HongKong Macao and Taiwan) Joint Laboratory on Advanced Materials Technologies, School of Materials Science and Engineering, Fuzhou University, Fuzhou 350108, China
[b] College of Material Sciences and Chemical Engineering, Harbin Engineering University, Harbin 150001, China

ARTICLE INFO

Article history:
Received 6 June 2023
Revised 29 June 2023
Accepted 12 July 2023
Available online 16 July 2023

Keywords:
Highly-chlorinated
Water/oxygen resistance
Stable interphase
Dendrite-free lithium metal batteries
High-rate

ABSTRACT

Side reactions and dendrite growth triggered by the unstable interface and inhomogeneous deposition have become the biggest obstacle to the commercialization for lithium metal batteries. In this study, a highly-chlorinated organic-inorganic hybrid interfacial protective layer is developed by rationally tuning the interfacial passivation and robustness to achieve the convenient and efficient Li metal anode. The polyvinyl chloride (PVC) can effectively resist water and oxygen, which is confirmed by density functional theory. The organic-dominant solid electrolyte interphases (SEI) with lithium chloride are investigated by the X-ray photoelectron spectroscopy (XPS) with little mineralization of oxide, such as Li_2O and Li_2CO_3. With such artificial SEI, a uniform and dense lithium deposition morphology are formed and an ultra-long stable cycle of over 500 h are achieved even at an ultra-high current density of 10 mA/cm^2. Moreover, the simple and convenient protected anode also exhibits excellent battery stability when paired with the $LiNi_{0.8}Co_{0.1}Mn_{0.1}O_2$ (NCM811) and $LiFePO_4$ (LFP) cathode, showing great potential for the commercial application of lithium metal batteries.

With the development of electric vehicles and energy storage technology, it is urgent to solve the problem of high-energy-density secondary batteries [1–6]. Lithium metal anode stands out among many anode materials for its lowest anode potential (−3.04 V *vs.* SHE) and ultra-high theoretical specific capacity of 3860 mAh/g [7–11]. However, there are several inherent problems with the practical use of lithium-metal batteries [12–14]. Due to the lowest chemical potential of lithium metal, it is difficult for lithium metal to exist in the organic electrolyte stably, forming a side reaction intermediate layer on the surface to prevent further reaction of lithium metal, and the intermediate layer is named SEI [15]. Unfortunately, the composition of the SEI layer generated *in situ* is complex and often breaks and regenerates during the cycle [16]. Such an SEI layer is not only difficult to inhibit dendrite growth, but also consumes a large amount of electrolyte, which brings serious capacity decay and safety hazards to lithium metal batteries [17–20]. Especially at high current densities, the cell will rapidly fail due to dendrite growth and the accumulation of a large number of side reaction products [21]. Therefore, it is necessary to develop a convenient and efficient artificial protective layer.

Ideally, the artificial protective layer would be stable in the electrolyte and passivate the lithium metal surface to reduce side reactions, provide uniform Li^+ transport channels to reduce dendrite generation, and have some mechanical strength to accommodate the inevitable volume changes [22,23]. To date, various inorganic passivation layers [24–27] have been used as artificial protective layers with high mechanical modulus and high ionic conductivity to inhibit dendritic crystal growth and side effects [28,29]. However, the inherent brittleness of mineralized inorganic layers makes it difficult to withstand the large volume changes of lithium metal [30]. The highly flexible organic polymer protective layer can perfectly adapt to the huge volume changes during electrode cycling [31–34]. However, the low mechanical strength of the organic layer makes it difficult to inhibit the growth of dendrites [35].

Constructing the SEI with organic and inorganic components can combine the advantages of both [36,37]. In this case, the inorganic component needs to be the optimal component to give the composite component high mechanical strength, good ionic conductivity and good toughness. In general, LiX (X = F, Cl, I) is the best choice [38–40]. Due to its insolubility, LiF is typically formed

* Corresponding authors.
E-mail addresses: zhiliangliu@hrbeu.edu.cn (Z. Liu), lilingyun@fzu.edu.cn (L. Li), yuyan@fzu.edu.cn (Y. Yu), chengkai_yang@fzu.edu.cn (C. Yang).

https://doi.org/10.1016/j.cclet.2023.108814
1001-8417/

by the decomposition of solvents or lithium salts. LiCl can be used as a powerful candidate [37,41,42], but it remains difficult to effectively add LiCl *in-situ* on the surface.

Here, we report the efficient and convenient use of PVC films as artificial layers to achieve stable cycling at high current densities. The crucial aspect of this protective layer is that during cycling, it generates a SEI layer rich in LiCl and chlorinated organic components. The anodes protected by the highly-chlorinated organic and inorganic SEI remain stable for a long period even at the water/oxygen environment, also confirmed by the density function theory (DFT). The interface stability is verified by XPS spectroscopy, which shows that there are almost no mineralization products Li_2O and Li_2CO_3 on the surface of the cycled lithium. In addition, by observing the deposition morphology through SEM, the dense, uniform and flat sediments are found, indicating that the protective layer has good surface leveling ability. The protected anode is capable of stable cycling over 500 h at ultra-high current densities of 10 mA/cm^2. With this SEI, both full-cell and half-cell cycling stability is greatly improved.

Artificial solid electrolyte interphases (ASEI) was prepared in an argon-filled glovebox with oxygen and H_2O below 0.5 ppm. A total of 5 mg of PVC were dissolved in 1 mL of tetrahydrofuran (THF), and the solution was dripped 20 μL onto Li and then dried on a heating table at 60 °C for 24 h to remove THF.

XPS measurements were performed on a Thermo ESCALAB 250 spectrometer, using non-monochromatic Al Kα X-rays as the excitation source and choosing C 1s (284.8 eV) as the reference line. The depth distribution was analyzed by Ar ion sputtering. Chemical information of SEI layer was collected after etching at 0 and 4 min. Scanning electron microscopy (SEM) was used to visualize the morphology of Li sediments and the thickness of ASEI (PVC drops are applied to stainless steel foil in the same process, the thickness and fracture morphology of ASEI were obtained by liquid nitrogen embrittleness.). The surface morphology of ASEI was observed using an atomic force microscope (AFM) by drop-coating PVC onto a copper foil for testing in air.

LFP is used as the cathode, which consists of 90 wt% LFP, 5 wt% polyvinylidene fluoride (PVDF) binder and 5 wt% super P Li (super P). The area mass load of LFP cathode is about 4 mg/cm^2. The operating potential window of the full battery is 2.8–4.2 V. NCM811 was used as the cathode. The cathode was composed of 90 wt% NCM811, 5 wt% PVDF adhesive and 5 wt% Super P. The mass load of NCM811 cathode was about 4 mg/cm^2. The operating potential window of the full battery is 2.8–4.25 V. All full battery evaluations were performed at room temperature. A Celgard 2300 separator, 50 μL of 1 mol/L $LiPF_6$ in the EC/DMC/EMC (1:1:1, v/v/v) with 5% FEC electrolyte, and Li anode with 0.25 mm thickness were employed in the full cells. The plating/stripping behavior of Li was accessed by symmetric Li cells (CR2032 coin cell) with 1 mol/L LiTFSI in DOL/DME (1:1, v/v) with 1% $LiNO_3$ electrolyte. Two pieces of Li foil were separated using a Celgard 2300 separator. All cathodes and anodes are 12 mm in diameter. The constant current discharge charging performance of half and full batteries was evaluated on the Neware Battery Test System (CT-4008) at room temperature. Electrochemical impedance spectroscopy (EIS) measurements were made using a CHI660D electrochemical workstation to achieve a 10 mV AC potential in the frequency range of 1000 kHz to 0.01 Hz. Cyclic voltammetry (CV) measurements were performed on CHI660 electrochemical station with a scanning range of −0.1 V to 0.1 V and a scanning rate of 10 mV/s.

DFT computations were performed using the Vienna ab initio simulation package (VASP). The interaction between the ionic core and valence electrons was described by the projector augmented wave method (PAW). The total energy convergence and the forces on each atom were set to be lower than 10^{-6} eV and 0.02 eV/Å. Energy cutoff of 500 eV for the plane wave basis set was used for the structure optimization. A 1 × 1 × 1 k-point mesh was used for the Brillouin zone sampling. The Predew-Burke-Ernzerhor functional with generalized gradient approximation was employed to describe the electron exchange and correlation energy. The adsorption energy was represented by ΔE, which is calculated by the following formula.

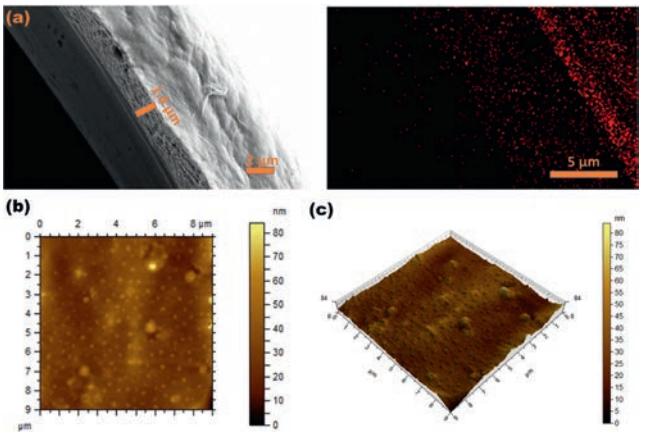

Fig. 1. (a) Cross-section and mapping of Li-PVC. (b) Two-dimensional AFM image of Li-PVC. (c) Three-dimensional AFM image of Li-PVC.

$$\Delta E = E_{total} - E_{slab} - E_{molecule} \quad (1)$$

where the E_{total} represents the energy of the whole after adsorption, the E_{slab} represents the energy of the adsorbed substrate, and the $E_{molecule}$ represents the energy of the adsorbed molecules.

The polyvinyl chloride is applied to the surface of lithium metal by the drip coating method to create an artificial protective layer. The manufacturing diagram is shown in Fig. S1 (Supporting information). The concentration optimization diagram is shown in Fig. S2 (Supporting information). After selecting the optimum drop coating concentration, the thickness of protective layer is about 1.4 μm in Fig. 1a, the PVC-coated Li was named Li-PVC. In Figs. 1b and c, the surface morphology was further studied using atomic force microscopy, and the 2D and 3D images showed that the coating on the Li metal surface is relatively smooth. Although there are some undulations, the height difference on the surface was only 86 nm, which can be considered as a uniform and smooth surface. The Young's modulus of PVC is much higher than that of the commonly used polymer polyethylene oxide indicating that PVC can be used as an organic robust surface (Fig. S3 in Supporting information).

The stability in a water/oxygen environment was tested by exposing bare lithium (bare Li) and Li-PVC in the air and water. Fig. 2a and Fig. S4 (Supporting information) showed that water and oxygen were effectively resisted by PVC, and the water was adhered stably on the Li-PVC. This indicates that the PVC coating is resistant to water/oxygen, which is helpful for the lithium metal to exit the argon atmosphere. As shown in Fig. S5 (Supporting information), the contact angles of ether-based and ester-based electrolytes on PVC surfaces are 31° and 28°, respectively, indicating that both electrolytes can wet the PVC surface well. The good wettability can ensure the stability of the electrode material and prevent the degradation of the cycle life caused by poor contact. To further verify the effectiveness of the water and oxygen resistance, bare Li and Li-PVC electrodes were subjected to long-term cycling after being exposed to air for five minutes. As shown in Fig. 2b, many black substances were generated on the surface of the bare Li electrode exposed to air, and the voltage hysteresis changes dramatically. In contrast, the Li-PVC electrode had a smooth and bright surface, and the voltage hysteresis remained stable for more

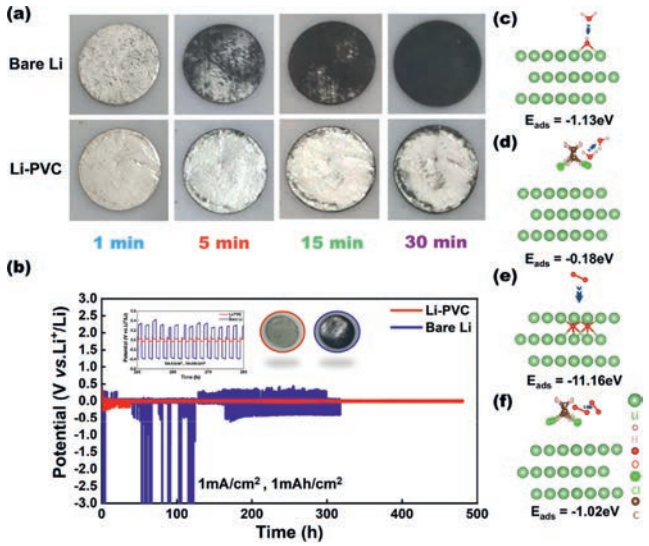

Fig. 2. (a) Bare lithium and Li-PVC exposed to air. (b) After exposure to air, the voltage curves of a symmetrical Li|Li cell were measured at a current density of 1 mA/cm^2 with a capacity of 1 mAh/cm^2. Atomic conformations and adsorption energy for H_2O species adsorption on (c) Li (111), and (d) Li (111) with PVC molecules (E_{ads} stands for adsorption energy). Atomic conformations and adsorption energy for O_2 species adsorption on (e) Li (111), and (f) Li (111) with PVC molecules. The arrow points from before to after structural optimization.

than 400 h, which clearly demonstrates the great commercial potential of this water and oxygen resistance capability. DFT was carried out to explore the water/oxygen resistance of PVC and its effect on lithium deposition. Figs. 2c and e showed the high reactivity of water and oxygen on lithium sheets. Water and oxygen on Li-PVC did not decompose and were repelled by PVC films away from the lithium surface (Figs. 2d and f). The adsorption energy also proved this point. The adsorption of water and oxygen on Li-PVC was much weaker than that of bare Li. Similarly, the adsorption energy of lithium atom on Li-PVC surface was 0.29 eV, and the adsorption energy of lithium atom on bare Li was −0.31 eV (Fig. S6 in Supporting information). This indicated that PVC passivated the Li metal interface and weaken the reaction of Li.

Next, XPS was applied to investigate the composition of the SEI on the surface of the lithium metal electrode after cycling (Figs. 3a and c). In the C 1s spectra, the peaks ascribed to C-C, C-O, and Li_2CO_3 were derived from the electrolyte. In the C 1s spectrum of Li-PVC, a larger part of the peaks assigned to C-C and C-H originated from PVC molecules, while C-O originated from the decomposition of the electrolyte. In the O 1s spectrum, Li_2O, C-O and C=O all come from the decomposition of electrolyte. In the F 1s spectrum, LiF originates from the decomposition of electrolyte, while C-F may originate from LiTFSI. Some LiCl is found in Cl 2p spectrum, LiCl is produced by PVC during the cycle. This indicates that the constructed SEI changes from all-organic components to organic and inorganic composite components in the cycle process. Fig. 3b shows the proportion of components in SEI. Remarkably, a small amount of LiF had been detected on the surface of Li deposited in the presence of PVC. In contrast, significant amounts of Li_2O and Li_2CO_3 were detected on the bare Li surface. There are up to five kinds of side reaction products on bare Li surface, while there are only four kinds of side reaction products on Li-PVC surface. The absence of traditional inorganic side reaction products indicates that Li-PVC electrode is more corrosion resistant. XPS of the Li-PVC electrode surface also exhibits similar results (Fig. S7 in Supporting information).

To understand the corrosion kinetics of Li anode, Tafel plots showed that Li-PVC exhibited lower exchange current density and higher Tafel slope compared to bare Li electrode, indicating that the composite anode produced fewer side reactions, which was consistent with the XPS results (Fig. 4a). CV was used to analyze the reaction kinetics of lithium metal batteries. The CV curves shown in Fig. 4b reflect the different electrochemical behaviors of the two electrodes. Compared with the bare Li electrode, the Li-PVC electrode exhibited a lower current, and the current varied linearly with the voltage, indicating that the redox process of Li-PVC was slower and more stable. To gain further insight into the nucleation and growth model in symmetric cells, a constant potential of −0.4 V was explored. From the time-current curve in Fig. 4c, the relaxation time of bare Li was 0.29 s. The relaxation time of Li-PVC was 0.7 s. It turns out that the nucleation rate on Li-PVC was slightly lower than that of Li sheets. The peak current of Li-PVC is lower than that of the bare Li electrode, indicating a slower growth rate of nuclei. And the $T_m \times I_m^2$ value of Li-PVC was higher than that of the bare Li electrode, which proved that the number of crystal nuclei on Li-PVC was higher than that of the bare Li electrode [43,44]. The impedance spectra before and after cycling are shown in Fig. S8 (Supporting information) and Fig. 4d, reflecting the SEI impedance and charge transfer impedance of the two electrodes. Due to the passivating ability of PVC, the SEI impedance and charge transfer impedance of Li-PVC are higher than bare Li before and after cycling. It is noteworthy that the SEI impedance and charge transfer impedance of bare Li and Li-PVC both decreased significantly after cycling. This is because LiF, Li_2O, and Li_2CO_3 become components of the SEI in bare Li during cycling, while LiF and LiCl become components of the SEI in Li-PVC, as inorganic components are known for their high ionic conductivity.

The electrodeposition of Li was further investigated using SEM characterization. After 50 cycles at 1 mA/cm^2, spatially inhomogeneous and highly porous Li dendrites were distributed on the bare Li electrode with a thickness of 100 μm depositions (Figs. 5a-c). In sharp contrast, the ion concentration gradient was mitigated on the Li-PVC and a slow but uniform interfacial ion migration was achieved, resulting in flat, dense, and dendrite-free Li deposited with a thickness of 75 μm (Figs. 5d-f). The results showed that this simple coating method was effectively applied to dendrite-free Li metal anodes. Based on the above research results, the schematic of Li^+ deposition on the bare Li and Li-PVC was shown in Fig. 5g. During the charging and discharging process of bare Li electrode, unstable SEI was formed, which could not inhibit dendrite growth and produce a lot of side reactions. However, the Li-PVC anode produced a stable SEI during the cycling process, which made the deposition smoother and the side reactions greatly reduced, so that the lithium anode withstood higher current density without forming dendrites.

The lithium plating/stripping performance of the PVC-protected lithium anode was investigated by galvanostatic cycling tests using a symmetric Li|Li battery. As shown in Fig. 6a, the symmetrical cells with Li-PVC anodes demonstrated excellent interfacial properties at current densities of 1 mA/cm^2 and lithium deposition capacity of 1 mAh/cm^2. Furthermore, the voltage profile of the Li-PVC anode was very stable even in cycling over 1000 h at a current density of 1 mAh/cm^2, and the high voltage hysteresis endowed the Li deposition with stronger controllability. However, the cells assembled with bare Li anode exhibited less voltage hysteresis. With the increase of cycle time, the voltage hysteresis greatly increased and the voltage plateau fluctuated significantly, which indicated that the unstable SEI was continuously broken/regenerated during the deposition/stripping process, and a large number of side reactants made the Li^+ transport difficult. Local short circuits due to uncontrolled deposition were observed at higher current densities of 3 mA/cm^2 (Fig. S9 in Supporting information). The staircase current density test also verified this, and compared to the

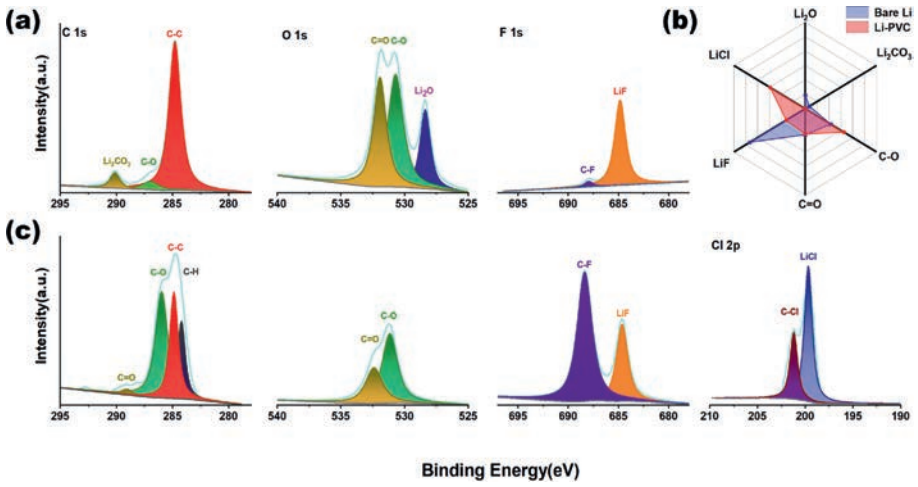

Fig. 3. (a) XPS spectra of the SEIs with the bare Li. (b) Distribution diagram of components in SEI. (c) XPS spectra of the SEIs with the Li-PVC (in-depth XPS).

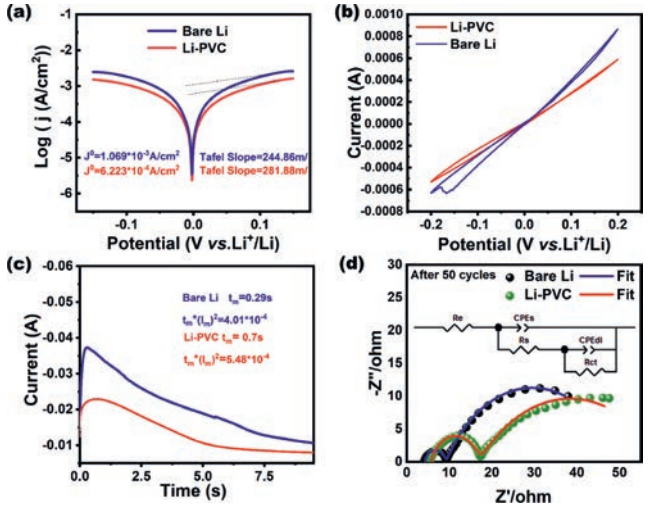

Fig. 4. (a) Tafel curves of Li symmetric cells. (b) CV curves. (c) Time current curves in the chronoamperometry. (d) Equivalent circuit of Nyquist diagram after 50 cycles (R_e is the body impedance, R_s is the SEI impedance, R_{ct} is the charge transfer impedance, and CPE is the constant phase element).

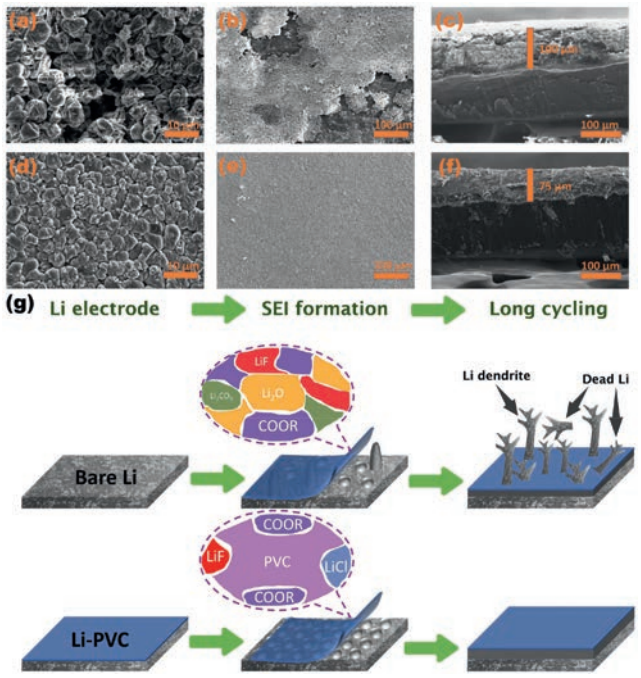

Fig. 5. (a, b, d, e) Top view and (c, f) cross view SEM images of Li deposits (1 mAh/cm^2, 1 mA/cm^2 after 50 cycles) on (a-c) bare Li and (d-f) Li-PVC. (g) Schematic illustrations of Li plating behavior.

bare Li electrode which is prone to short-circuiting, the Li-PVC electrode exhibits extremely high stability during the process of current density changes (Fig. S10 in Supporting information). Remarkably, the Li-PVC anode achieved stable Li plating/stripping for 500 h at an extremely high current density of 10 mA/cm^2 in symmetrical cells, while the bare Li anode exhibited a significant accumulation of side reactions resulting in a sharp increase in voltage hysteresis after approximately 200 h (Fig. 6b). This demonstrates the strong application potential of the layer under high current density conditions. To evaluate the application prospects of the PVC protective layer in practical batteries, Li-PVC anodes were assembled with LFP to form Li metal full batteries. Li-PVC exhibited better cyclability. Specifically, the Li-PVC||LFP coin cell exhibited an average coulombic efficiency of 99.9% over 290 cycles at 0.5 C and exhibited a capacity retention rate of 96% (Fig. 6c). By comparison, the bare Li||LFP coin cell showed a low-capacity retention of 79% after 290 cycles, which was attributed to the increase in cell impedance caused by the massive accumulation of side reaction products. Moreover, the Li-PVC||LFP coin cell exhibits equally excellent performance at a 5 C rate, with virtually no capacity degradation within the first 100 cycles (Fig. S11 in Supporting information). In addition, NCM811 batteries exhibited the same properties (Fig. S12 in Supporting information). Specifically, the Li-PVC||NCM811 coin cell exhibited a capacity retention of 74% after 170 cycles at 1 C. By comparison, the bare Li||NCM811 coin cell exhibited a low-capacity retention of 56% after 170 cycles. Compared to the Bare Li electrode, the Li-PVC electrode exhibits higher discharge specific capacity recovery during the transition from high to low rates, indicating that the Li-PVC has superior rate performance (Fig. S13 in Supporting information). The comparison of this work with other reports in Fig. 6d [45–50], where all works used ether electrolytes with added lithium nitrate and a fixed areal capacity of 1 mAh/cm^2. It can be observed that Li-PVC exhibits excellent performance at high current density, surpassing most of the studies. This indicates that the Li-PVC strategy is promising for high current density applications.

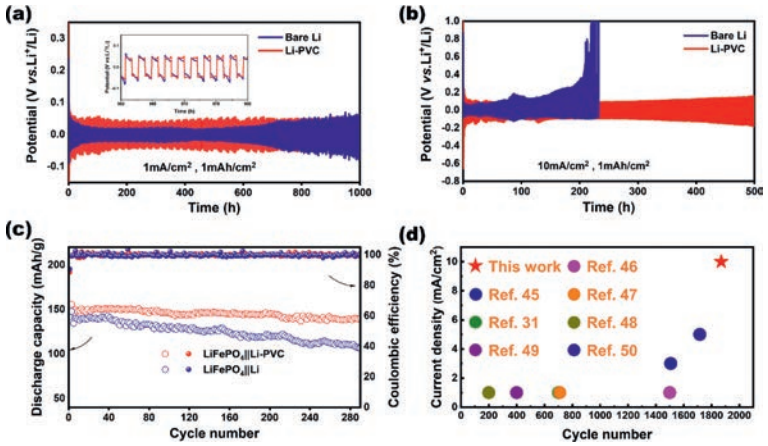

Fig. 6. (a, b) Symmetric Li|Li coin cell curve in a wide range of current density with a fixed capacity of 1 mAh/cm^2. (c) Li||LFP and Li-PVC||LFP coin cell in the current density of 0.5 C under long-term cycle performance. (d) The comparison of this work with other reports.

In conclusion, we have developed a passivated and robust interface for dendrite-free and efficient Li metal anodes. The interface is very simple and practical to make, and it can exist stably in the air and can be used for mass production. During the cycle, the PVC-protected electrode derived SEI rich in LiCl and organic components. The SEI of this component is achieved in the near absence of oxide mineralized products, such as Li_2O and Li_2CO_3, to provide a stable and passivated interface. In addition, the stable layer affects the reaction kinetics of the lithium deposition and forms uniform Li^+ diffusion and dendrite-free deposition. As a result, at a current density of 10 mA/cm^2, the symmetric Li|Li cells exhibit excellent performance. The LFP full-cell performance with almost no degradation also demonstrates the potential application of the protected anode. This work clarifies the importance of passivating the interface to stabilize lithium metal anodes, which may be a promising and low-cost strategy for developing safer and more stable high-rate Li metal anodes.

Declaration of competing interest

The authors declare that they have no known competing financial interests or personal relationships that could have appeared to influence the work reported in this paper.

Acknowledgments

This work was supported primarily by National Natural Science Foundation of China (Nos. 22109025, 51972061), National Key Research and Development Program of China (No. 2020YFA0710303), Natural Science Foundation of Fujian Province, China (No. 2021J05121).

Supplementary materials

Supplementary material associated with this article can be found, in the online version, at doi:10.1016/j.cclet.2023.108814.

References

[1] X. Zhang, Y. Yang, Z. Zhou, Chem. Soc. Rev. 49 (2020) 3040–3071.
[2] B. Liu, J.G. Zhang, W. Xu, Joule 2 (2018) 833–845.
[3] S. Chu, Y. Cui, N. Liu, Nat. Mater. 16 (2017) 16–22.
[4] C. Yang, R. Shao, Q. Wang, et al., Energy Stor. Mater. 35 (2021) 62–69.
[5] C. Yang, R. Shao, Y. Mi, et al., J. Power Sources 376 (2018) 200–206.
[6] S. Yang, B. Wang, Q. Lv, et al., Chin. Chem. Lett. 34 (2022) 107783.
[7] D. Lin, Y. Liu, Y. Cui, Nat. Nanotechnol. 12 (2017) 194–206.
[8] G. Xu, R. Li, M. Li, et al., Chem. Eng. J. 434 (2022) 134498.
[9] B. Li, Y. Chao, M. Li, et al., Electrochem. Energy R. 6 (2023) 7.
[10] J. Liu, H. Yuan, H. Liu, et al., Adv. Energy Mater. 12 (2022) 2100748.
[11] L. Zhai, K. Yang, F. Jiang, et al., J. Energy Chem. 79 (2023) 357–364.
[12] Y. Liu, Q. Liu, L. Xin, et al., Nat. Energy 2 (2017) 1–10.
[13] C. Yan, X.B. Cheng, Y. Tian, et al., Adv. Mater. 30 (2018) 1707629.
[14] K. Yang, L. Li, Y. Xiao, et al., Chin. Chem. Lett. 35 (2024) 108451.
[15] S. Li, J. Huang, Y. Cui, et al., Nat. Nanotechnol. 17 (2022) 1–9.
[16] Y. Han, B. Liu, Z. Xiao, et al., InfoMat 3 (2021) 155–174.
[17] Q. Wang, C. Yang, J. Yang, et al., Adv. Mater. 31 (2019) 1903248.
[18] J. Guo, Y. Chen, Y. Xiao, et al., Chem. Eng. J. 422 (2021) 130526.
[19] C. Li, Y. Li, Z. Chen, et al., Chin. Chem. Lett. 34 (2023) 107852.
[20] Y. Xiao, X. Wang, K. Yang, et al., Energy Stor. Mater. 55 (2023) 773–781.
[21] A. Hu, W. Chen, X. Du, et al., Energy Environ. Sci. 14 (2021) 4115–4124.
[22] R. Xu, X.B. Cheng, C. Yan, et al., Matter 1 (2019) 317–344.
[23] Z. Yu, Y. Cui, Z. Bao, Cell Rep. Phys. Sci. 1 (2020) 100119.
[24] A.C. Kozen, C.F. Lin, A.J. Pearse, et al., ACS Nano 9 (2015) 5884–5892.
[25] Y.H. Tan, G.X. Lu, J.H. Zheng, et al., Adv. Mater. 33 (2021) 2102134.
[26] H. Chen, A. Pei, D. Lin, et al., Adv. Energy Mater. 9 (2019) 1900858.
[27] K. Chen, R. Pathak, A. Gurung, et al., Energy Stor. Mater. 18 (2019) 389–396.
[28] C. Gao, Q. Dong, G. Zhang, et al., ChemElectroChem 6 (2019) 1134–1138.
[29] Z. Chen, B. Wang, Y. Li, et al., ACS Appl. Mater. Interfaces 14 (2022) 28014–28020.
[30] R. Xu, Y. Xiao, R. Zhang, et al., Adv. Mater. 31 (2019) 1808392.
[31] R. Lu, A. Shokrieh, C. Li, et al., Nano Energy 95 (2022) 107009.
[32] N.W. Li, Y. Shi, Y.X. Yin, et al., Angew. Chem. Int. Ed. 57 (2018) 1505–1509.
[33] K. Liu, A. Pei, H.R. Lee, et al., J. Am. Chem. Soc. 139 (2017) 4815–4820.
[34] Y. Sun, Y. Zhao, J. Wang, et al., Adv. Mater. 31 (2019) 1806541.
[35] X. Liu, J. Liu, T. Qian, et al., Adv. Mater. 32 (2020) 1902724.
[36] F. Liu, Q. Xiao, H.B. Wu, et al., Adv. Energy Mater. 8 (2018) 1701744.
[37] Q. Zhao, Z. Tu, S. Wei, et al., Angew. Chem. 130 (2018) 1004–1008.
[38] J. Tan, J. Matz, P. Dong, et al., Adv. Energy Mater. 11 (2021) 2100046.
[39] J. Yang, C. Hu, Y. Jia, et al., ACS Appl. Mater. Interfaces 11 (2019) 8717–8724.
[40] Y. Lin, Z. Wen, J. Liu, et al., J. Energy Chem. 55 (2021) 129–135.
[41] X. Liang, Q. Pang, I.R. Kochetkov, et al., Nat. Energy 2 (2017) 1–7.
[42] D. Zeng, J. Yao, L. Zhang, et al., Nat. Commun. 13 (2022) 1909.
[43] A.I. Danilov, E.B. Molodkina, Y.M. Polukarov, Russ. J. Electrochem. 36 (2000) 1236–1244.
[44] Y. Liu, C. Tan, Z. Jia, et al., J. Cent. South Univ. (Sci. Technol.) 41 (2010) 144–149.
[45] X.F. Liu, D. Xie, F.Y. Tao, et al., ACS Appl. Mater. Interfaces 14 (2022) 23588–23596.
[46] B. Han, Y. Zou, R. Ke, et al., ACS Appl. Mater. Interfaces 13 (2021) 21467–21473.
[47] Q. Jin, X. Zhang, H. Gao, et al., J. Mater. Chem. A 8 (2020) 8979–8988.
[48] S. Guo, N. Piao, L. Wang, et al., ACS Appl. Energy Mater. 3 (2020) 7191–7199.
[49] H. Wang, L. Wu, B. Xue, et al., ACS Appl. Mater. Interfaces 14 (2022) 15214–15224.
[50] P. Chen, L. Li, C. Wang, et al., Appl. Surf. Sci. 604 (2022) 154468.